Combined Theoretical and Experimental Investigation and Design of H_2S Tolerant Anode for Solid Oxide Fuel Cells

Final Technical Report
Start Date: July 21st 2005
Project End Date: July 20th 2008

Gerardine G. Botte (Primary Contact), Damilola Daramola, Madhivanan Muthuvel
Date Issued: October 2008

Award Number: DE-FG26-05NT42527

Ohio University
Office of Research and Sponsored Programs
105 Research and Technology Center
Athens, OH, 45701

DISCLAIMER

ABSTRACT

A solid oxide fuel cell (SOFC) is a high temperature fuel cell and it normally operates in the range of 850 to 1000°C. Coal syngas has been considered for use in SOFC systems to produce electric power, due to its high temperature and high hydrogen and carbon monoxide content. However, coal syngas also has contaminants like carbon dioxide (CO_2) and hydrogen sulfide (H_2S). Among these contaminants, H_2S is detrimental to electrode material in SOFC. Commonly used anode material in SOFC system is nickel-yttria stabilized zirconia (Ni-YSZ). The presence of H_2S in the hydrogen stream will damage the Ni anode and hinder the performance of SOFC. In the present study, an attempt was made to understand the mechanism of anode (Ni-YSZ) deterioration by H_2S. The study used computation methods such as quantum chemistry calculations and molecular dynamics to predict the model for anode destruction by H_2S. This was done using binding energies to predict the thermodynamics and Raman spectroscopy to predict molecular vibrations and surface interactions. On the experimental side, a test stand has been built with the ability to analyze button cells at high temperature under syngas conditions.

TABLE OF CONTENTS

EXECUTIVE SUMMARY

A SOFC is a high temperature fuel cell which operates at temperatures between 850 and 1,000°C. The SOFC is a viable option for a high temperature hydrogen fuel source. One of the high temperature hydrogen sources is coal syngas. Burning coal produces a gas known as coal syngas, which contains hydrogen along with other chemical species such as CO and CO_2. Since an SOFC operates at high temperature, the presence of CO and CO_2 in coal syngas will not affect its performance. A commonly used anode material for SOFCs is Ni-YSZ. When H_2S-containing gas comes in contact with a Ni-based anode, deterioration of the anode is inevitable. Most of the experimental research in the area of SOFCs has been focused on development of new anode materials for sustaining H_2S attack. In this project, we concentrate on understanding the mechanism of anode (Ni-YSZ) deterioration by H_2S gas present in the coal syngas, using molecular modeling. We also want to establish validity for the predicted theoretical models by experimental analysis. Hence, objectives for this project are to determine the mechanism for H_2S interaction with the Ni-YSZ anode and recommend either preventive measures for the Ni-YSZ anode or a new sulfur tolerant anode material.

This study was performed to provide better understanding of the mechanism for SOFC anode deterioration by H_2S gas found in coal syngas. To do this, an investigation of the interactions of the anode with chemical species would lead to a methodology. This methodology allows the combination of theoretical models with experiments and surface analysis to elucidate the H_2S attack on anode material. Based on these objectives, the study was able to establish a methodology predicting the thermodynamics of Ni-YSZ anode in the presence of H_2, H_2S and CO. Calculated binding energies (using Gaussian version 03) for the interactions between the anode and a molecule of H_2, H_2S and CO were found to be -80.1, -21.4 and -23.9 kcal/mol respectively. This indicated that the H_2 interaction is the most favorable while the H_2S interaction is the least favorable. In addition, for a mixture of gas molecules, the binding energies were -21.6, -155.5 and -134.6 kcal/mol for H_2+H_2S, H_2+CO and CO+H_2S respectively. This further strengthens the conclusion that the presence of H_2S is not favorable for oxidation of H_2 on the surface of the anode molecule. These results were published in the Electrochemical and Solid-State Letters (2006) found attached.

In addition, it was determined that periodic calculation based on vibrational analysis of the non-periodic structure of the electrolyte was necessary to complete the optimization of anode structure. This was required as the calculated and experimental Raman spectra for Ni-YSZ were not identical. After an X-ray diffraction analysis on the electrolyte (YSZ) sample, it was confirmed that the electrolyte indeed possessed the cubic form. Therefore, periodic calculations would help in accurately predicting the crystal structure and its vibrational spectroscopy. Upon switching to periodic calculations (using CRYSTAL version 06), the results had better agreement with experimental results. A study of monoclinic ZrO_2 showed bond angles and lengths in agreement within 2° and 0.05Å. More importantly, calculated Raman spectra showed 13 frequency modes matching and these were within an average difference of 12 cm^{-1}. These results can also be further extended to YSZ and the anode (Ni-YSZ). These results have been submitted for publication in the Journal of Computational Chemistry (2008).

Finally, an experimental setup for testing SOFC anodes in the presence of H_2S and other contaminants has been built. This experimental setup has been optimized for a button cell with a diameter between 26 and 32 mm and can go to a maximum temperature of 900°C. Due to time constraints, experimental analysis could not be performed, however included in this report is a test matrix for 8 button cells. These cells will be tested at an OCV between 0.2 and 0.7 V and the results will be reported in an addendum to this final report to be submitted by February 2009.

REPORT DETAILS

Approach

Initial quantum chemistry calculations were performed using Gaussian 03. Binding energies were calculated with the anode material (NiO-YSZ) and molecules of hydrogen, hydrogen sulfide and carbon monoxide. These binding energies showed that thermodynamically, the presence of hydrogen sulfide in the system was unfavorable. However, it was important that the structure be experimentally validated and Raman spectroscopy was employed for this validation. When the Gaussian calculated Raman spectrum for the electrolyte was compared to the experimental spectrum, there were huge discrepancies in the peaks observed. In addition, the use of XRD analysis showed that this material had a cubic structure due to stabilization by yttrium oxide. At this point, the structure was revised to represent a periodic structure. This revision was begun from the monoclinic ZrO_2 and then would later be extended to the cubic yttria-stabilized electrolyte and then the nickel-oxide yttria-stabilized zirconia.
In the experimental analysis, an experimental setup was built which would test button cells with 30mm diameter and electrodes of 10mm diameter. The anode and cathode are Ni-YSZ and LSM-YSZ respectively. The current collectors to be used are silver mesh on the cathode side and nickel mesh on the anode side. In addition, Pt paste will be applied to both sides to ensure proper attachment between the current collectors and the electrodes. A test matrix is attached which will be used to test these button cells at the OCVs mentioned earlier.

Results

Theoretical Analysis
Based on the values in table 1, the presence of H_2S in the system hinders oxidation of carbon monoxide and hydrogen. This is in agreement with experimental details as the anode performs less effectively with H_2S present.

Table 1

Systems	Binding Energy (kcal/mol)
H_2	-80.1
H_2S	-21.4
CO	-23.9
$H_2 + H_2S$	-21.6
$H_2 + CO$	-155.5
$H_2S + CO$	-134.6

On comparing the vibrational spectroscopy of monoclinic ZrO_2 and the electrolyte with experimental results [2,3] (Figure 1 & 2), there were discrepancies in the peaks observed.

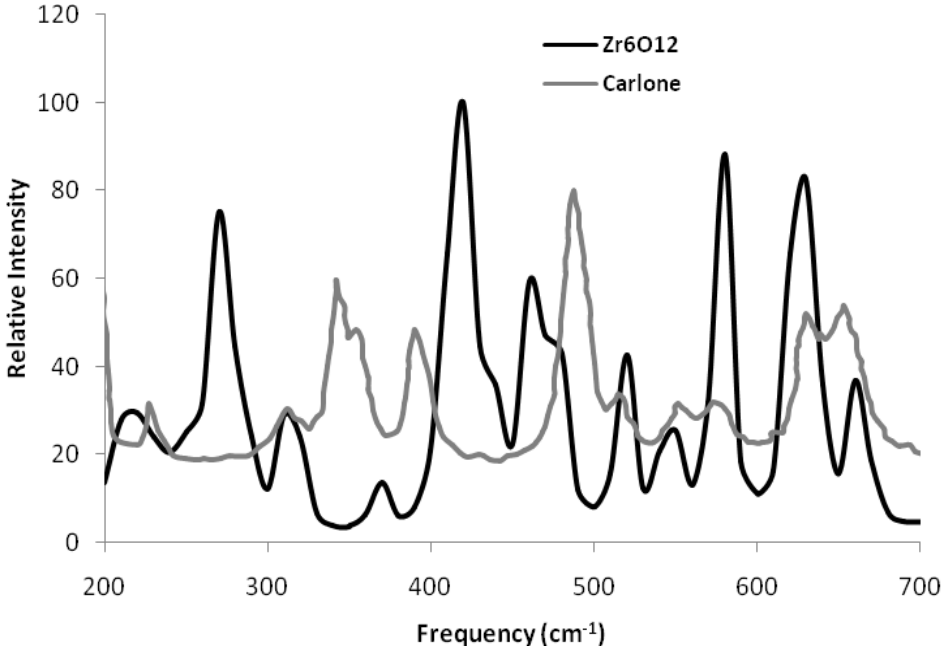

Figure 1

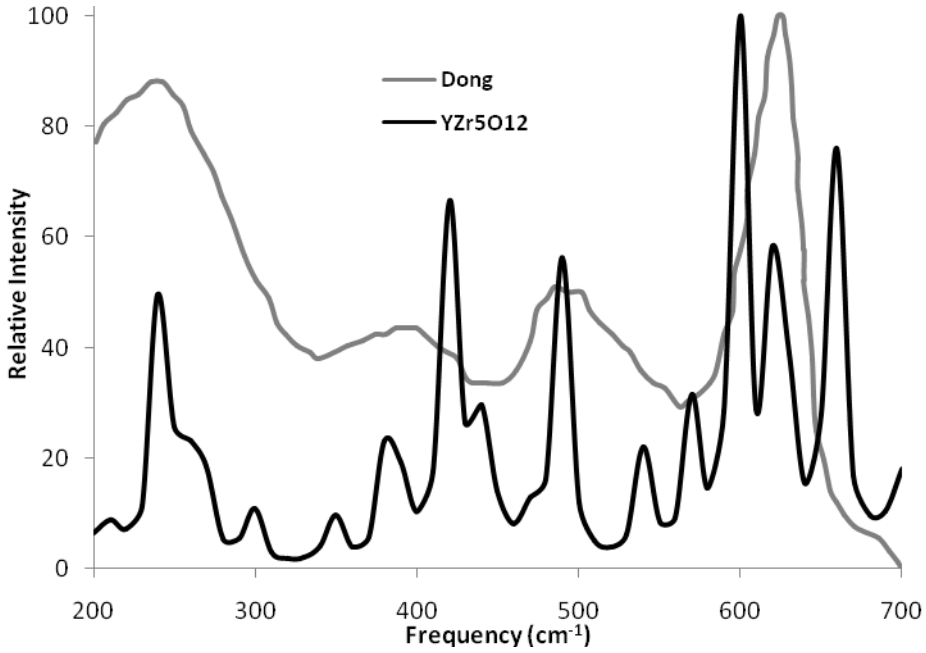

Figure 2

This result, combined with XRD analysis shows that the SOFC electrolyte has a cubic structure suggested that a revision in the theoretical analysis was necessary.

Using CRYSTAL (version 06) [4], the monoclinic ZrO_2 was calculated using the B3LYP level of theory. The lattice parameters (unit cell dimensions, angle, and atom coordinates) were calculated and compared to experimental values to ensure that the calculated structure was valid. The average percent difference was 1.27% for lattice parameters [5] while the bond angles and lengths were within 0.05Å and 2° respectively [6]. A frequency analysis was performed on the calculated

structure and the mean average difference calculated was 12 cm^{-1} (Table 2). This was based on 14 agreed frequency modes for monoclinic zirconia.

Table 2

Experimental	**Our Work**	**Difference**
ω (cm^{-1})	ω (cm^{-1})	Δ
102	74	-28
	182	
179	182	3
190	199	8
223	226	4
	328	
305	340	35
334	351	17
347	364	16
381	387	6
	394	
476	487	12
501	509	8
536	570	34
558	574	17
615	638	22
637	651	14
	775	
Average Difference		12

These results compared well with the accuracy found with other theoretical methods. In addition, Figure 3 shows a visual comparison between the experimental and theoretical vibration spectrum. It is evident that this is in better agreement than the previously optimized structure in figure 1.

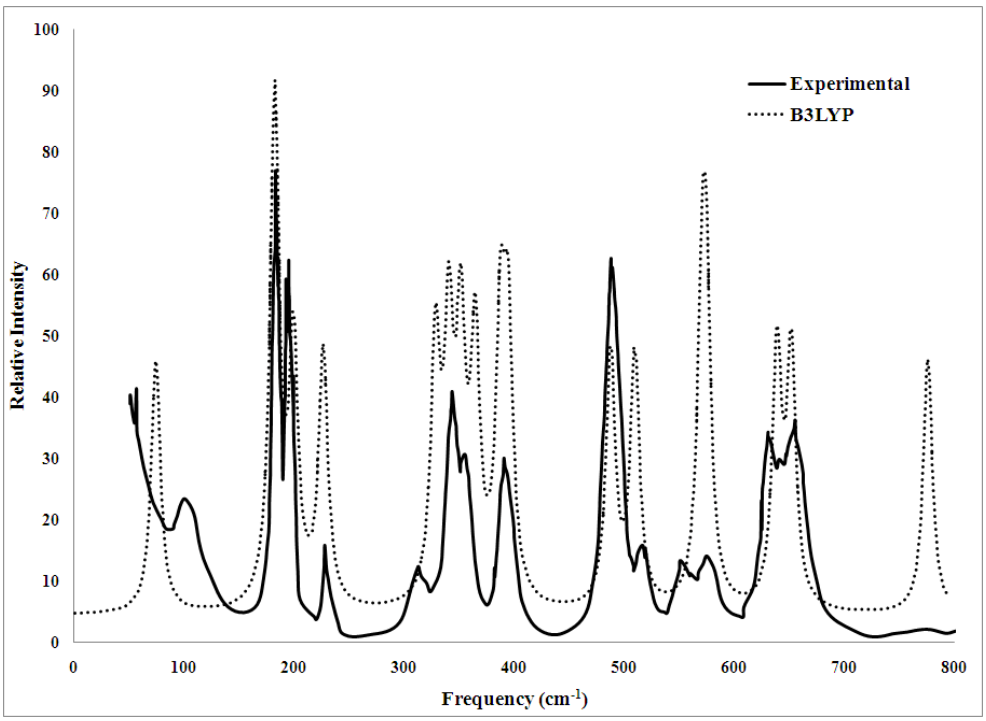

Figure 3

The success of predicting the monoclinic ZrO_2 showed that with proper modification, a similar structure could be generated for the cubic yttria-stabilized form of zirconia.

Experimental Analysis

For the experimental analysis, the building of the test stand is now complete. Problems related to tape-casting, design of cell housing and mesh attachment have all been resolved and a pilot experimental matrix has been made (Table 2). This matrix is based on a 0.5 hydrogen fuel utilization and maximum load of 1000 mA/cm^2. Under these conditions, the anode side flow would be $48cm^3$ while the cathode side flow would be $57cm^3$. The runs are based on 0.1, 0.5 and 1 ppm of H_2S with nitrogen as the carrier gas and a constant H_2 mole fraction of 0.25.

Experiment	Component	Mol Fraction	Flow rate (cm^3/min)
#1	**H_2**	0.25	11.94
	N_2	0.75	35.83
	Air		56.87
#2	**H_2S**	1.00E-07	11.94
	H_2	0.25	0.24
	N_2	0.75	35.59
	Air		56.87
#3	**H_2S**	5.00E-07	11.94
	H_2	0.25	1.19
	N_2	0.75	34.63
	Air		56.87
#4	**H_2S**	1.00E-06	11.94
	H_2	0.25	2.39
	N_2	0.75	33.44
	Air		56.87
#5	**H_2**	0.25	11.94
	N_2	0.75	35.83
	Air		56.87
#6	**H_2S**	1.00E-07	11.94
	H_2	0.25	0.24
	N_2	0.75	35.59
	Air		56.87
#7	**H_2S**	5.00E-07	11.94
	H_2	0.25	1.19
	N_2	0.75	34.63
	Air		56.87
#8	**H_2S**	1.00E-06	11.94
	H_2	0.25	2.39
	N_2	0.75	33.44
	Air		56.87

Conclusions and Future Directions

- Based on prior analysis, it is required that the models used be validated experimentally at every step using experimental methods such as XRD and Raman spectroscopy.
- The agreement between lattice parameters and frequency modes and symmetry can be translated to success in other structures being calculated at the same level of theory.
- Based on the success of the methodology found, it is recommended that further investment becomes available to extend the models to other materials and systems to understand and improve the performance of SOFCs
- The experimental setup is robust enough to handle the high temperature due to the use of platinum paste to hold current collectors to screen-printed electrodes.
- Future calculations will be performed on the cubic structure of YSZ and Ni-YSZ.

- The experimental tests projected will be reported in an appendix/addendum to this report to account for the experimental analysis that could not be performed due to time constraints.

Graphical Materials List

References

1. J. Dong, Z. Cheng, S. Zha, M. Liu, *J. Power Sources*, **156** 461 (2006)
2. C. Carlone, *Phys Rev B* **45** 2079 – 2084 (1992)
3. R. Dovesi, V.R. Saunders, C. Roetti, R. Orlando, C.M. Zicovich-Wilson, F. Pascale, B. Civalleri, K. Doll, N.M. Harrison, I.J. Bush, Ph. D'Arco, M. Llunell, CRYSTAL06 User's Manual, University of Torino, Torino. (2006)
4. C.J. Howard, R.J. Hill, B.E. Reichert, *Acta Crystallographica B* **44**, 116 (1988)
5. J. D. McCullough, K. N Trueblood, *Acta Crystallographica*, **12**, 507-511(1959)
6. B.K. Kim, H.O. Hamaguchi, *Phys Status Solidi B-Basic Res*, **203**, 557-563 (1997).

Acronyms

SOFC: Solid Oxide Fuel Cell
Ni-YSZ: Nickel in Yttria-Stabilized Zirconia
LSM-YSZ: Lanthanum Strontium Manganite in Yttria-Stabilized Zirconia
XRD: X-ray Diffraction Analysis

Appendices

1. A.I. Marquez, Y. De Abreu, G.G. Botte, Electrochem Solid State Lett 2006, **9**, A163-A166 (2006)
2. D. Daramola, M. Muthuvel, G.G. Botte, **Theoretical Analysis of Raman Frequency Modes of Monoclinic Zirconia**, *submitted to Journal of Computational Chemistry (October 2008).*

Electrochemical and Solid-State Letters, **9** (3) A163-A166 (2006)
1099-0062/2006/9(3)/A163/4/$20.00 © The Electrochemical Society

Theoretical Investigations of NiYSZ in the Presence of H_2S

Andres I. Marquez,* Yolanda De Abreu,* and Gerardine G. Botte*,z

Russ College of Engineering and Technology, Ohio University, Athens, Ohio 45701, USA

Quantum chemistry and molecular dynamics were used to evaluate the performance of solid oxide fuel cell anode materials in the presence of H_2 and H_2S. The most common anode material Ni-yttria-stabilized zirconia (Ni-YSZ) was used for the study. It was found that the presence of H_2S has an important effect on the oxidation of H_2. Thermodynamics and transport limitations favor the oxidation of H_2 instead of H_2S. Furthermore it is predicted that the presence of H_2S slows down the oxidation of the hydrogen due to transport limitations (the H_2S molecules tend to be surrounded by H_2 molecules in the media).
 [DOI: 10.1149/1.2165708]

Manuscript submitted September 26, 2005; revised manuscript received November 25, 2005.
Available electronically January 18, 2006.

Solid oxide fuel cells (SOFCs) seem to be the most viable fuel cell technology to handle coal-derived syngas, as they are able to stand contaminants such as carbon monoxide (CO) and carbon dioxide (CO_2) which are present in the syngas. However, coal-syngas also contains hydrogen sulfide (H_2S) at high concentrations (between 0.5 and 5% H_2S depending on where the coal is mined).[1] The presence of this contaminant in coal-syngas is one of the major obstacles to implementing a coal-syngas SOFC, since an anode catalyst able to handle the presence of H_2S without deterioration over time has not been developed. Several attempts, based on traditional trial-and-error experimental methods, have been made in order to develop an anode material that can withstand the presence of hydrogen sulfide in the fuel.[2-18] The literature review indicates that many issues are still unclear regarding the screening of some materials for the oxidation of the H_2S present in the coal-derived syngas: (*i*) screening of the materials has been performed at different conditions and therefore it is difficult to compare the results available in the literature; (*ii*) the stability of the materials during time has not been studied in depth; (*iii*) the mechanisms that lead to the deactivation of the electrode material are unknown; and (*iv*) the effect of H_2S and other contaminants present in the coal-syngas on the performance of the anode materials has not been determined. In order to develop a sulfur-tolerant anode it is necessary to fill in information about all these gaps. Molecular modeling seems to be an excellent tool to achieve this as it can be used to gain a better understanding of the performance of the materials and to guide the experimental work.

Few attempts have been made to use molecular modeling to understand the structure of electrolyte materials for SOFC applications.[19-40] Several researchers have used molecular dynamics simulations and quantum chemistry discrete Fourier transform (DFT) methods to study several properties (such as material deformation, grain growth, plasticity, ionic conductivity, grain boundary phenomena, oxide ion O^{2-} diffusion, among others) and to develop better zirconia-based electrolyte materials, such as yttria-stabilized zirconia (YSZ).[19-40] However, to date no studies that deal with molecular modeling of high-temperature anode materials for solid oxide fuel cell applications and their interactions with the gas-phase components of the coal-syngas (H_2, H_2S, H_2O, CO, CO_2, etc.) have been found in the open literature.

This paper is the first of a series of publications that focus on investigating the mechanisms of anode deterioration due to the presence of H_2S in the syngas fuel for solid oxide fuel cells by using molecular modeling [quantum chemistry (QC) and molecular dynamics (MD)]. Within this context, the objective of this paper is to examine the interactions of Ni-YSZ in the presence of hydrogen and hydrogen sulfide. Ni-YSZ was selected for this study as it is the most common anode used in SOFCs.

* Electrochemical Society Active Member.
z E-mail: botte@ohio.edu

Methodology

QC calculations.— The chemical interactions and the reactivity of H_2 and H_2S with the selected electrode material (Ni-YSZ) were determined by using first principles modeling (ab initio). First principles modeling uses the laws of quantum mechanics as the basis for their calculations, yielding the energy and other properties of a system after geometry optimizations are performed. Geometry optimization calculations were performed to locate the lowest energy molecular structure associated with the specified starting configuration.[41-43] *Gaussian 03*[41,42] was used for all the QC calculations at the b3pw91/lanl2dz level of theory, which combines a density functional theory (DFT)[44] method and the basis set LANL2DZ.[41,42] DFT methods offer some of the benefits of computationally expensive and accurate methods such as ab initio at a practically low computational cost that is comparable to semiempirical methods.[41,42] One of the advantages of DFT methods is that they include the effects of electron correlation in the model.[41,42] The basis set LANL2DZ was selected due to the presence of atoms beyond the third row of the periodic table (Ni, Y, Zr). It is worthwhile to point out that attempts were made to compare the results of the chosen method and basis set with less robust methods and basis sets (e.g., HF/6-311G* level of theory was tested to optimize the YSZ and the Ni-YSZ clusters); however, the optimizations did not run successfully in *Gaussian 03*[41] due to the presence of Y, Zr, and Ni.

The cluster size of the simulated Ni-YSZ anode material was determined by several factors: (*i*) the composition of the anode (actual experimental composition was chosen, the widely used YSZ composition is ZrO_2 85–97%-Y_2O_3 3–15%);[35-40] (*ii*) the effectiveness in the computational time (QC calculations limit the cluster size due to the long computational time required for the optimization of the molecules), and (*iii*) the chemical stability of the simulated electrode structure (the cluster size chosen guaranteed that the simulated solid phase mimicked the surface region of the Ni-YSZ material with no major bulk effects). Thus, a cluster of at least 12 atoms was modeled using the crystallographic properties of zirconia-based ceramic materials.[45]

MD simulations.— MD simulations[46,47] were performed to determine diffusion coefficients of the gas species interacting with the electrode material, identify structural variations at each phase (gas and solid phases), and determine packing and orientation of the chemical species at the surface of the electrode material. Packing and orientation of the chemical species were determined from the radial distribution functions (RDF), and diffusion coefficients were calculated through the mean square displacement.[46,47] The software Cerius2 and the universal force field (UFF),[48] corrected with all the optimized molecules parameters obtained from QC calculations (DFT method), were used for the MD studies. The computations were performed in a SGI IRIX workstation. The UFF is a purely harmonic and diagonal force field, in which the nonbond interactions are handled via a Leonard-Jones potential for the van der Waals interactions and a coulombic term for the electrostatic

interactions.[39,40,48,49] This force field has been successfully used and proven to adequately simulate several systems in similar studies[39] and other applications.[49]

A constant number of particles, volume, and temperature (NVT) ensemble, or canonical ensemble, was used.[46,47] The temperature was controlled using Berendsen's method.[48-50] The simulations were performed at three different temperatures (25, 600, and 850°C). Each simulation began with 5000 fs of equilibration using a 0.5-fs/iteration time step and the velocity scaling temperature control method. Molecular dynamics simulations were continued for an additional 200 ps using a 0.5-fs/iteration time step until equilibration was achieved. Successful equilibration was judged by plotting both the running and batch averages for the total energy vs time. Equilibrium was reached when the batch-average energies oscillated smoothly around the constant running-average energy. The simulation time allowed obtaining sufficient data from the trajectory and velocity histograms, which were saved with a frequency of 5 fs as reported by others.[40,49] 3D periodic unit cells of at least 8000 $Å^3$ in volume were constructed to ensure having enough number of atoms (hundreds and thousands) for the solid phase as well as to simulate the real density for the gas-phase stream.

Results and Discussion

Ni-YSZ anode structure optimization.— A ZrO_2 cluster containing 6 Zr atoms and 12 oxygen atoms was optimized according to the structure reported in the literature,[45] the optimized cluster was used to build the electrolyte molecule as described next. The unit cell structure for simulating the YSZ cluster was built and optimized by substituting a zirconium (Zr) atom with an yttrium (Y) atom (see Fig. 1a), as it has been performed in similar studies.[35-38] Table I contains details of some the more important distances, bond lengths, and angles for this and the other optimized systems. The optimized YSZ structure also simulates the oxygen vacancy encountered when adding yttria to zirconia.[35-38]

NiO was added to the optimized electrolyte cluster YZr_5O_{12} (YSZ) at the top region close to the Y atom (see Fig. 1b). This configuration was found to be the most stable in our studies. It can be noticed from Fig. 1b that there is a six-atom ring formed after the NiO is attached to the YSZ, favoring the stability of the Ni-YSZ. This ring was formed after the atoms O10 and Zr7 (Fig. 1a) broke their bond, and then each bonded to the approaching Ni19-O20 (O10 to Ni19 and Zr7 to O20, respectively), as it is depicted in Fig. 1b. Moreover, the bond lengths involved in the six-atom ring are similar (ranging from 1.78 to 2.28 Å, see Table I), indicating a stable configuration. A large binding energy value (see Table II) of −130 kKcal/mol for the resultant structure confirms that the structure is stable and the presence of NiO greatly promotes the attachment of Ni into the YSZ structure. This suggests that the NiO-YZrO system can reasonably represent the anode material Ni-YSZ; therefore it was used as the representative cluster of the Ni-YSZ anode material.

Interactions anode-gas phase.— The interactions of the optimized anode structure with either H_2, H_2S, or both at the same time (Fig. 2) were separately evaluated. For simplicity, the final configurations for the H_2 and H_2S cases are not shown. Table II summarizes the binding energies of the different systems. The binding energy for the Ni-YSZ-H_2 system (−80.1 kcal/mol) is almost four times lower than for the Ni-YSZ-H_2S system (−21.4 kcal/mol). The energy of the Ni-YSZ-H_2/H_2S system (−21.6 kcal/mol) is the same as the Ni-YSZ-H_2S system. These results suggest that the oxidation of H_2 is thermodynamically preferred at the anode. However, the oxidation of H_2S is also thermodynamically feasible. The optimization of the combined system consisting of Ni-YSZ, one molecule of H_2, and one molecule of H_2S (see Fig. 2) was performed in order to evaluate the simultaneous reactivity of each molecule toward the anode structure. The binding energy value suggests that the H_2S slows down the reactivity (oxidation) of H_2 molecules towards the surface of the Ni-YSZ anode.

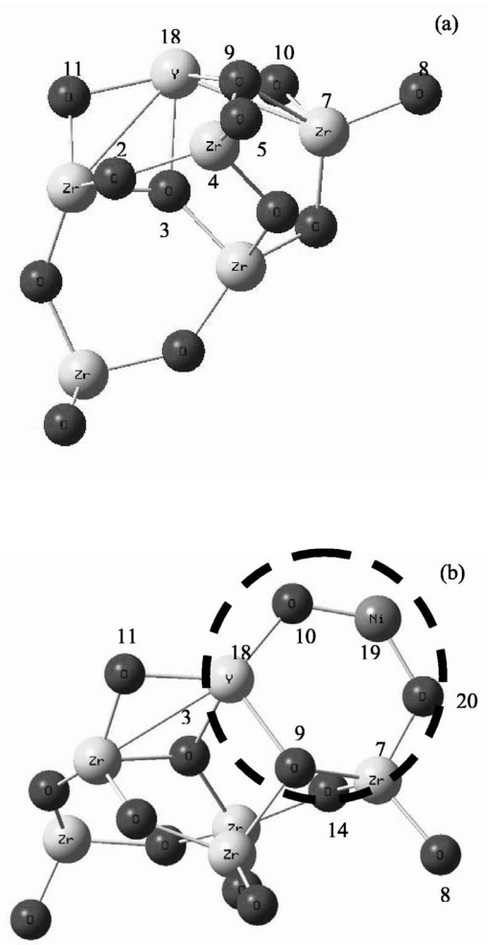

Figure 1. Optimized structures for the electrolyte and electrode material: (a) electrolyte YZr_5O_{12} and (b) anode NiO-YZr_5O_{12}. (The marked six-atom ring, formed by the atoms Y18-O10-Ni19-O20-Zr7-O9, is almost planar except for atoms O9 and Zr7 that go slightly out/in of the plane, respectively.)

Comparison of the variation of the distances and angles (see Table I) in the different systems can be used to predict reactivity of the gases (H_2 and H_2S) with the electrode. The increase in the separation distances of Y18-Ni19 and O9Ni19 (for the system in Fig. 1b to the system in Fig. 2) from 3.36 and 3.73 Å to 3.44 and 3.92 Å, respectively, indicates strong Ni interactions with the gas-phase components (H_2 and H_2S). This can also be corroborated by looking at the angle variation; for example, the Y18-O10-Ni19 angle increases in the Ni-YSZ-H_2/H_2S system (125.9°) when compared to the Ni-YSZ (120.9°). Although the figures are not shown, it is worthwhile to mention that for the H_2 alone and H_2S alone cases a variation of the bond lengths/distances and angles of the Ni, Y, and adjacent O atoms was also observed. For the H_2 case, it was detected that the separation distance between the H_2 molecule and the O8 and O20 atoms was 0.97 Å, which indicates the tendency of a bond formation; moreover, an increase in the internal Ni-Y (Y18-Ni19) distance from 3.36 to 3.41 Å (see Fig. 1b), shows the strong interaction of the H_2 towards the anode surface. On the other hand, for the case of H_2S the distance Ni-S (Ni19-S22, Fig. 2) was 2.48Å and the internal separation Ni-Y (Y18-Ni19) increased from 3.36 to 3.41 Å, similar to the H_2 case; this shows that the H_2S oxidation is also thermodynamically feasible but is less favored than for the H_2 molecules.

Table I. Distances, bond lengths, and angles predicted by the QC calculations. The numbers used in the atoms refer to Fig. 1 and 2.

System	Atomic pair	Distance/bond length (Å)[a]	Atomic trio	Angle (°)
YZr_5O_{12} (YSZ)	Zr7-O8	2.02	O10-Zr7-O8	110.6
	Y18-O10	2.15	O11-Y18-O10	159.0
	Y18-O9	2.14	O9-Y18-O10	76.1
	Y18-O11	2.15	O11-Y18-O9	112.8
	Y18-O3	2.31	O3-Y18-O11	73.5
	Y18-Zr7	3.16	Y18-Zr7-O8	137.4
NiO-YZr_5O_{12} (Ni-YSZ)	Zr7-O8	2.03	O11-Y18-O10	126.7
	Zr7-O9	2.07	O11-Y18-O9	126.2
	Zr7-O20	1.93	O9-Y18-O10	107.1
	Y18-O10	2.08	O9-Zr7-O8	117.3
	Y18-O9	2.28	O9-Zr7-O20	107.2
	Y18-O11	2.14	Y18-O9-Zr7	115.7
	Y18-Ni19	3.36	Ni19-O20-Zr7	121.8
	Ni19-O20	1.82	O10-Ni19-O20	128.4
	Ni19-O10	1.78	Y18-O10-Ni19	120.9
	Ni19-O9	3.73	O20-Zr7-O8	111.6
	Ni19-Zr7	3.28	O9-Ni19-O20	60.0
NiYSZ + H_2 + H_2S	Y18-O10	2.08	O9-Zr7-O8	118.4
	Y18-O11	2.14	Y18-O9-Zr7	112.9
	Y18-O9	2.28	O9-Zr7-O20	107.7
	Y18-Ni19	3.44	Y18-O10-Ni19	125.9
	Ni19-O20	1.88	Ni19-O20-Zr7	127.3
	Ni19-O10	1.77	O10-Ni19-O20	118.6
	Ni19-O9	3.92	O9-Ni19-O20	54.7
	Ni19-Zr7	3.40	O20-Zr7-O8	135.0

[a] When two atoms are not bonded the values refer to separation distance.

Molecular dynamics studies.— MD computations were performed for understanding of the interactions between the atoms of the anode material and the atoms of the environment (H_2 and H_2S). Figure 3 shows the radial distribution function (RDF) of the different components of the anode material (Ni, Zr, Y, and O) when only hydrogen is present in the environment at ambient temperature (25°C). The maximum RDF is denoted by the pair Ni-H. These data indicate that hydrogen prefers to be sited adjacent to Ni ions which will favor the H_2 oxidation on the Ni sites. On the other hand, when the temperature is increased to 600 and 850°C, similar results in the RDF and atoms distances were obtained for the pairs Zr-H, Y-H, and O-H. However, for the pair Ni-H, the situation was different. It was found that the height of these peaks (Ni-H) increased with increasing the temperature, which indicates that the oxidation of H_2 is enhanced by increasing the temperature (the concentration of H atoms is higher at the Ni sites, that is, diffusion limitations are minimized).

Molecular dynamics simulations were also performed in a H_2S/H_2 environment at 850°C. A snapshot of the simulations is given in Fig. 4. When H_2S is present in the environment, the RDF Ni-H peak is smaller than the one without H_2S at the same temperature, and is closer (shorter distance Ni-H) than the Ni-S pair case (distance Ni-S longer), indicating that the H_2S is less attracted to the surface than hydrogen and the hydrogen moves slower in the presence of H_2S. This in agreement with the quantum chemistry results presented before, and also suggests that the H_2S oxidation could start taking place but at a slower rate than H_2 oxidation due to transport limitations. Moreover, the proximity of H_2 and S atom (of H_2S) to the Ni atom of the surface of the anode cluster clearly suggests that there is an strong interaction of the Ni atoms of the anode material with the H_2 and H_2S species in the gas phase, and that the anode material could start degrading due to the loss of Ni atoms, as it has been well established in the experimental studies found in the literature.[2-18]

Table II. Binding energies predicted by the QC calculations for the different systems.

System	Binding energy (kcal/mol)
NiO-YZr_5O_{12} (Ni-YSZ)	−130.0
Ni-YSZ + H_2	−80.1
Ni-YSZ + H_2S	−21.4
Ni-YSZ + H_2 + H_2S	−21.6

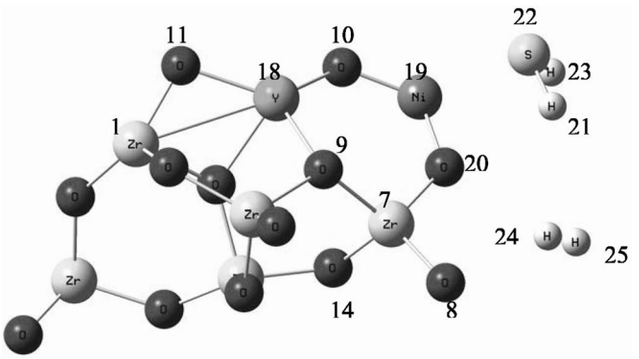

Figure 2. Optimized Ni-YSZ + H_2 + H_2S system: anode NiO-YZr_5O_{12} interacting with one H_2 and one H_2S molecule.

The diffusivities of the species were determined from the MD studies at different temperatures, and the results are shown in Table III. The diffusion coefficients of H_2 in the gas phase on the anode material were found to increase when increasing temperature. On the other hand, when H_2S is present in the mixture, the diffusion coefficient of hydrogen decreased significantly when compared to pure H_2. For example, from Table III it can be noticed that the diffusivity of hydrogen in the presence of H_2S was on the order of 1.10×10^{-4} cm^2/s at 850°C (which is 20% lower than for H_2 alone). It was also found that the diffusion coefficient of H_2S is always lower than the one for H_2, for example, at 850°C the diffusivity of H_2S is 1×10^{-5} cm^2/s. Moreover, in agreement with the RDF results, it is clear that the H_2S molecules tend to be surrounded by H_2 molecules, which, as it has been said before, could slow down the oxidation of hydrogen.

Conclusions

Quantum chemistry and molecular modeling can provide useful information for determining favorable materials for the anode electrode of SOFCs and its stability in the oxidation medium. This work

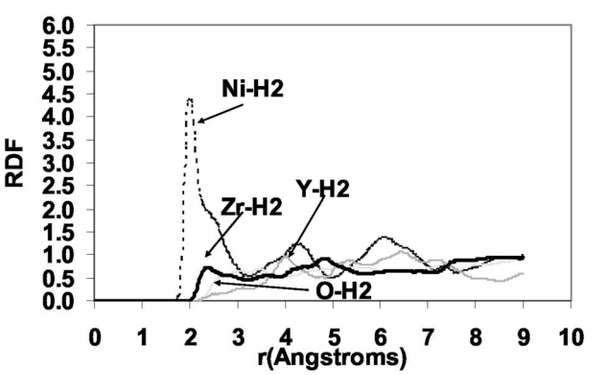

Figure 3. Radial distribution function for Y, Zr, Ni, and O atoms (anode) with H_2 gas phase at 25°C.

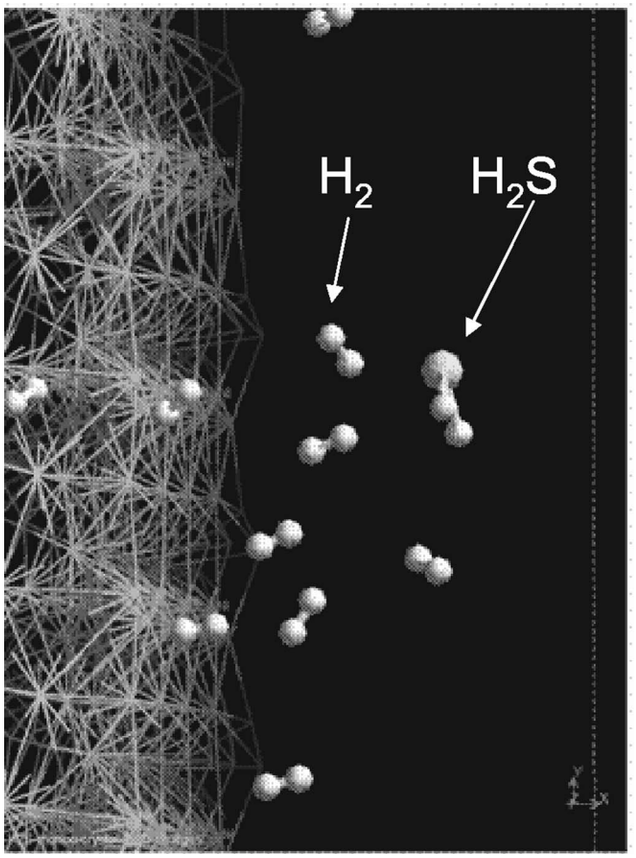

Figure 4. Interaction of H_2 and H_2S with the Ni in the anode material at 850°C.

Table III. Diffusion coefficients of the gas-phase components predicted by the MD simulations.

Temperature (°C)	Diffusivity H_2 (cm^2/s)	Diffusivity of H_2 in a H_2/H_2S mixture (cm^2/s)	Diffusivity of H_2S in a H_2/H_2S mixture (cm^2/s)
25	10^{-7}		
600	10^{-6}		
850	1.34×10^{-4}	1.1×10^{-4}	1×10^{-5}

serves as a basis for future development and design of sulfur–tolerant anode materials for SOFC application. Comparison of the predicted modeling results with experimental studies will be presented in future publications.

The results also show that the simulated Ni-YSZ cluster size mimics with great certainty the solid surface of those materials, as essentially no variation in bond lengths and angles were observed in the bulk atoms (Zr, O) that form part of those materials during the quantum chemistry and MD studies. Thermodynamics and transport limitations favor the oxidation of H_2 instead of H_2S. Transport limitations slow down the oxidation of H_2 in a H_2/H_2S mixture.

Acknowledgments

This work was supported by Ohio University (Postdoctoral Fellowship Award through the Vice President for Research Office).

Ohio University assisted in meeting the publication costs of this article.

References

1. G. Y. Lai, *High Temperature Corrosion of Engineering Alloys*, p. 117, ASM International, Materials Park, OH (1990).
2. N. U. Pujare, K. W. Semkow, and A. F. Sammells, *J. Electrochem. Soc.*, **134**, 2639 (1987).
3. R. J. Bouchard, P. A. Russo, and A. Wold, *Inorg. Chem.*, **4**, 685 (1965).
4. N. U. Pujare, K. J. Tsai, and A. F. Sammells, *J. Electrochem. Soc.*, **136**, 3662 (1989).
5. I. V. Yentekakis and C. G. Vayenas, *J. Electrochem. Soc.*, **136**, 996 (1989).
6. T. J. Kirk and J. Winnick, *J. Electrochem. Soc.*, **140**, 3494 (1993).
7. D. R. Peterson and J. Winnick, *J. Electrochem. Soc.*, **145**, 1449 (1998).
8. C. Yates and J. Winnick, *J. Electrochem. Soc.*, **146**, 2841 (1999).
9. Y. Matsuzaki and I. Yasuda, *Solid State Ionics*, **132**, 261 (2000).
10. M. Liu, P. He, J. L. Luo, A. R. Sanger, and K. T. Chuang, *J. Power Sources*, **94**, 20 (2001).
11. P. He, M. Liu, J. L. Luo, A. R. Sanger, and K. T. Chuang, *J. Electrochem. Soc.*, **149**, A808 (2002).
12. M. Liu, G. L. Wei, J. Luo, A. R. Sanger, and K. T. Chuang, *J. Electrochem. Soc.*, **150**, A1025 (2003).
13. G. L. Wei, M. Liu, J. L. Luo, A. R. Sanger, and K. T. Chuang, *J. Electrochem. Soc.*, **150**, A463 (2003).
14. G. L. Wei, J. Luo, A. R. Sanger, and K. T. Chuang, *J. Electrochem. Soc.*, **151**, A232 (2004).
15. S. Wang, M. Liu, and J. Winnick, *J. Solid State Electrochem.*, **5**, 188 (2001).
16. L. Aguilar, S. Zha, Z. Cheng, J. Winnick, and M. Liu, *J. Power Sources*, **135**, 17 (2004).
17. L. Aguilar, S. Zha, S. Li, J. Winnick, and M. Liu, *Electrochem. Solid-State Lett.*, **7**, A324 (2004).
18. R. Mukundan, E. L. Brosha, and F. H. Garzon, *Electrochem. Solid-State Lett.*, **7**, A5 (2004).
19. F. Haase and J. Sauer, *J. Am. Chem. Soc.*, **120**, 13503 (1998).
20. C. A. J. Fisher and H. Matsubara, *Solid State Ionics*, **113-115**, 311 (1998).
21. C. A. J. Fisher and H. Matsubara, *Comput. Mater. Sci.*, **14**, 177 (1999).
22. C. A. J. Fisher and H. Matsubara, *J. Eur. Ceram. Soc.*, **19**, 703 (1999).
23. H. Ogawa, N. Sawaguchi, and F. Wakai, *Mater. Sci. Forum*, **243-245**, 351 (1997).
24. H. Ogawa, N. Sagawuchi, and F. Wakai, *Mater. Sci. Forum*, **357-359**, 571 (2001).
25. H. Ogawa and F. Wakai, *Mater. Trans., JIM*, **42**, 2266 (2001).
26. F. Wakai, N. Kondo, and H. Ogawa, *Mater. Charact.*, **37**, 331 (1996).
27. S. Ostanin, A. J. Craven, D. W. McComb, D. Vlachos, A. Alavi, M. W. Finnis, and A. T. Paxton, *Phys. Rev. B*, **62**, 728 (2000).
28. G. Jomard, T. Petit, and A. Pasturel, *Phys. Rev. B*, **59**, 4044 (1999).
29. W. C. Mackrodt and P. M. Woodrow, *J. Am. Ceram. Soc.*, **69**, 277 (1986).
30. M. Kilo, C. Argirusis, G. Borchardt, and R. A. Jackson, *Phys. Chem. Chem. Phys.*, **5**, 2219 (2003).
31. G. Staper, M. Bernasconi, N. Nicoloso, and M. Parinello, *Phys. Rev. B*, **59**, 797 (1999).
32. M. S. Khan, M. S. Islam, and D. R. Bates, *J. Mater. Chem.*, **8**, 2299 (1998).
33. A. S. Foster, V. B. Sulimov, F. L. Gejo, A. L. Shluger, and R. M. Nieminen, *Phys. Rev. B*, **64**, 224108 (2001).
34. S.-H. Chen, Y.-S. Yin, D.-P. Wang, and J. Li, *J. Cryst. Growth*, **267**, 100 (2004).
35. Y. Yamamura, S. Kawasaki, and H. Sakai, *Solid State Ionics*, **126**, 181 (1999).
36. S. Fabris, A. T. Paxton, and M. W. Finnis, *Acta Mater.*, **50**, 5171 (2002).
37. Y. W. Tang, Q. Zhang, and K.-Y. Chan, *Chem. Phys. Lett.*, **385**, 202 (2004).
38. T. Arima, K. Fukuyo, K. Idemitsu, and Y. Inagaki, *J. Mol. Liq.*, **113**, 67 (2004).
39. Pradip and B. Rai, *Colloids Surf., A*, **205**, 139 (2002).
40. L. R. Martins and M. S. Skaf, *J. Phys. Chem. B*, **108**, 19687 (2004).
41. M. J. Frisch, G. W. Trucks, H. B. Schlegel, G. E. Scuseria, M. A. Robb, J. R. Cheeseman, J. A. Montgomery, Jr., T. Vreven, K. N. Kudin, J. C. Burant, J. M. Millam, S. S. Iyengar, J. Tomasi, V. Barone, B. Mennucci, M. Cossi, G. Scalmani, N. Rega, G. A. Petersson, H. Nakatsuji, M. Hada, M. Ehara, K. Toyota, R. Fukuda, J. Hasegawa, M. Ishida, T. Nakajima, Y. Honda, O. Kitao, H. Nakai, M. Klene, X. Li, J. E. Knox, H. P. Hratchian, J. B. Cross, V. Bakken, C. Adamo, J. Jaramillo, R. Gomperts, R. E. Stratmann, O. Yazyev, A. J. Austin, R. Cammi, C. Pomelli, J. W. Ochterski, P. Y. Ayala, K. Morokuma, G. A. Voth, P. Salvador, J. J. Dannenberg, V. G. Zakrzewski, S. Dapprich, A. D. Daniels, M. C. Strain, O. Farkas, D. K. Malick, A. D. Rabuck, K. Raghavachari, J. B. Foresman, J. V. Ortiz, Q. Cui, A. G. Baboul, S. Clifford, J. Cioslowski, B. B. Stefanov, G. Liu, A. Liashenko, P. Piskorz, I. Komaromi, R. L. Martin, D. J. Fox, T. Keith, M. A. Al-Laham, C. Y. Peng, A. Nanayakkara, M. Challacombe, P. M. W. Gill, B. Johnson, W. Chen, M. W. Wong, C. Gonzalez, and J. A. Pople, *Gaussian 03*, ed. Gaussian Inc., Wallingford, CT (2004).
42. E. Frisch, M. J. Frisch, and G. W. Trucks, *Gaussian 03 User's Reference*, ed. Gaussian Inc., Pittsburgh, PA (2003).
43. G. H. Grant and W. G. Richards, *Computational Chemistry*, O.S. Publications, Oxford (1995).
44. A. Marquez, A. Vargas, and P. B. Balbuena, *J. Electrochem. Soc.*, **145**, 3328 (1998).
45. R. W. G. Wyckoff, *Crystal Structure*, Vol. 2, 2nd ed., Wiley, New York (1961).
46. M. P. Allen and D. J. Tildesley, *Molecular Dynamics Simulation of Liquids*, John Wiley & Sons. New York (1992).
47. J. M. Haile, *Molecular Dynamics Simulation. Elementary Methods*, John Wiley & Sons, New York (1992).
48. Accelrys, Cerius^2, Accelrys, San Diego, CA (2003).
49. A. Marquez and P. B. Balbuena, *J. Electrochem. Soc.*, **148**, A624 (2001).
50. H. J. C. Berendsen, J. P. M. Postma, W. F. V. Gunsteren, A. D. Nola, and J. R. Haak, *J. Chem. Phys.*, **81**, 3684 (1984).

Theoretical Analysis of Raman Frequency Modes of Monoclinic Zirconia

Introduction

Zirconium Oxide (Zirconia) in its various forms has been used as a gem, furnace and refractory lining and as a solid electrolyte. This is due to its stability to heat and chemical influences[1]. Zirconia exists in three main phases: monoclinic ($P2_1/c$) at ambient conditions, tetragonal ($P4_2/nmc$) at temperatures greater than 1440 K and cubic (Fm3m) at temperatures above 2600K[2]. Each of these materials has been studied extensively, however the focus will be on the experimental[3-8] and theoretical[9-14] analyses of the monoclinic structure.

The experimental analyses have investigated geometry[3], measured lattice parameters[7] and vibrational spectra[4-6,8]. As far back as 1959, McCullough was able to measure the bond angles and lengths accurately within experimental standard deviations of 2° and 0.05Å respectively[3]. Bondars et. al used both X-ray analysis and neutron diffraction to calculate the lattice parameters and found that the values varied slightly between samples and method of analysis, within a maximum of 2 experimental standard deviations[7]. Anastassakis, Papinacolaou and Asher examined and listed 12 Raman frequency modes for monoclinic zirconia ranging from 177 cm^{-1} to 616 cm^{-1} although according to group theory, 18 modes are expected ($9A_g + 9 B_g$)[4]. Ishigame and Sakurai examined the effect of temperature on the Raman spectra and found that as the temperature increased, there was a shift to lower frequencies i.e. a red shift and a broadening of the peaks[5]. This became more pronounced at 1420K as the peaks for monoclinic phase begin to weaken in intensity and the peaks for the tetragonal phase begin to increase. This process occurs in reverse when the temperature is decreased. Feinberg and Perry further extended this study by investigating the effect of the concentration of an impurity on the Raman modes[6]. It was noted that the increase in impurity concentration caused a blue shift in frequency. The authors noted 14 Raman modes (also less than the projected 18 modes) and assigned the symmetry of the modes using Ishigame's method. Recently, Kim & Hamaguchi performed an analysis on the Raman modes using isotopic exchanges to examine the atoms causing each vibration mode. These were assigned as Zr-O, Zr-Zr and O-O stretches.

In regards to theoretical analyses, most were performed using plane wave basis sets. Dewhurst and Lowther studied monoclinic zirconia in relation to other phases existing at high pressures and temperatures including α-PbO_2 (Pbcn), rutile ($P4_2/mnm$), anatase ($I4_1/amd$), brookite (Pbca) and cotunnite ($Pca2_1$)[9]. Christensen and Carter performed spin restricted calculations using the Local Density Approximation (LDA) to Density Functional Theory (DFT) on surfaces of the 3 common phases. Their results correctly predicted the monoclinic structure as the ground phase and found surface entropies which agreed with experimental values on the order of 0.4 mJ/m^2K [14]. Jomard et al. using the LDA and generalized gradient corrected (GGC) functionals of Perdew-Wang (PW91) and Perdew-Becke (PB) calculated lattice parameters, cohesive energies and band gap for monoclinic ZrO_2. The GGC functionals overestimated the lattice parameters and energies; on the other hand, while the LDA functional overestimated the energy by 15%, the GGA functional overestimated this value by 7%. This is expected as GGAs in general improve predictions of lattice parameters and energies [15]. Gennard, Cora and Catlow performed calculations on bulk cubic Zirconia and provided the basis for the tolerances and shrink factors to be used in this work as their studies were performed using Gaussian basis sets. The work performed by Zhao and Vanderbilt was the first found to include calculated Raman and Infrared frequencies along with lattice parameters and energy using an LDA functional based on the Ceperley-Alder correlation. The frequency modes found were compared to those of earlier authors[4,16] and found to correctly predict the trend, although it was suggested that some modes be reassigned. Kuwabara et al.[12] used the PW91 functional and also were able to predict IR and Raman spectra in close agreement with previous theoretical and experimental work[5,13,16].

The purpose of this study is to generate vibrational spectra of monoclinic ZrO_2 as a platform for the molecular modeling of a solid oxide fuel cell (SOFC). A typical SOFC consists of yttrium doped zirconia (YSZ) as the electrolyte and nickel combined with this doped electrolyte as the anode (Ni-YSZ)[17]. A previous study by Marquez, De Abreu and Botte looked at the effect of hydrogen sulfide on the anode of a typical SOFC using quantum chemistry and molecular modeling[18]. Using a hybrid functional (B3PW91), they were able to predict the binding energies of Ni-YSZ with combinations of hydrogen and

hydrogen sulfide and these energies showed that the oxidation of H_2S is thermodynamically less feasible. Bond angles and lengths are also listed within this paper; however these have not been validated experimentally. Consequently, this work is being done to

1. Test Gaussian basis sets to be used in predicting structural and vibrational characteristics of zirconia, beginning with the monoclinic phase.
2. Establish a background for combining theoretical and experimental studies of SOFC components using vibrational spectroscopy.

These two objectives will be the foundation on which future investigations involving SOFC components will be based.

Methodology

The bulk of the computational calculations were performed using CRYSTAL 06[19] with additional analysis performed in Gaussian 03[20] for a better understanding of the system under non-periodic conditions.

In Crystal, the widely used B3LYP[21,22] hybrid functional was the method of calculation employed. This functional has been found to perform well in previous frequency calculations for both molecular and periodic solid state systems[23-25]. The basis set used to describe the Zr atom uses the Hay and Wadt Small Core effective core potential to replace the 28 inner core electrons and reduce computational demand[26]. On the other hand, two different basis sets previously used in zirconia studies by Bredow[27] (labeled B.S. B) and Gennard et al.[10] (labeled B.S. G) are being used for oxygen. These basis sets are highlighted in detail in Table 1 with the coefficients and exponents of each orbital. Based on the review in the previous section, a shrinking factor of 4X4X4 was used resulting in 30 k-points in the initial Brillouin zone. The SCF total energy convergence tolerance (TOLDEE) was set to 10^{-10} hartree (default value is 10^{-6}) as was the norm in other frequency calculations using Crystal. Structures were visualized using Moldraw[28,29].

In Gaussian, B3PW91[30] was the method of calculation used. This was the same method of calculation employed by Marquez, De Abreu and Botte in the previous work and is used for ease of comparison with their work. The LANL2DZ basis set was used to describe the entire molecule using the Los Alamos ECP

for zirconium and the D95V basis set for oxygen. All other values were set to the default for calculation and the visualization of calculated structures was done using GaussView[31].

Table 1: Oxygen Basis Sets used in CRYSTAL 06 calculations

Orbital	B.S. B[32]			B.S. G[10]		
	Exponents	*Coefficients*		*Exponents*	*Coefficients*	
1s	8020	0.00108		4000	0.00144	
	1338	0.00804		1355.58	0.00764	
	255.4	0.05324		248.545	0.0537	
	69.22	0.1681		69.5339	0.16818	
	23.9	0.3581		23.8868	0.36039	
	9.264	0.3855		9.27593	0.38612	
	3.851	0.1468		3.82034	0.14712	
	1.212	0.0728		1.23514	0.07105	
2sp	49.43	-0.00883	0.00958	52.1878	-0.00873	0.00922
	10.47	-0.09150	0.06960	10.3293	-0.08979	0.07068
	3.235	-0.04020	0.20650	3.21034	-0.04079	0.20433
	1.217	0.37900	0.34700	1.23514	0.37666	0.34958
3sp	0.50000	1.00000	1.00000	0.53642	1.00000	1.00000
4sp	0.19100	1.00000	1.00000	0.21000	1.00000	1.00000
d	0.65000	1.00000		0.50000	1.00000	

Results and Discussion

Geometry Optimization

The monoclinic phase of ZrO_2 has each Zr atom with a 7-fold coordination, an oxygen with a 3-fold coordination (labeled as O_1) and the other with a 4-fold coordination (labeled O_2). The unit cell is shown in figure 1 with O_1 and O_2 labeled.

Based on comparison between the calculated lattice parameters using the two basis sets for O and the B3LYP functional in comparison (Table 2), the experimental values (averages from Bondars et al. samples) and previously calculated values using LDA and GGA functional, the average percentage differences were 1.27% and 1.67% for B.S B and B.S. G respectively. On the other hand, the plane wave basis sets yielded 0.73% and 1.57% for the LDA and the GGA functional respectively.

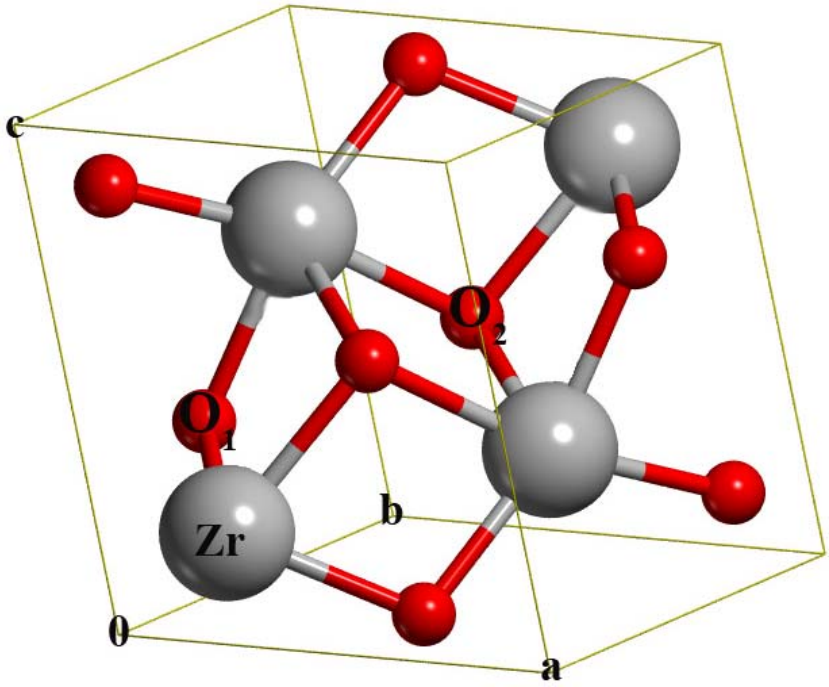

Figure 1. Fully Optimized unit cell for Monoclinic ZrO_2

Table 2: Lattice parameters

Parameters	B.S. B	B.S. G	LDA[13]	GGA[12]	Expt[7]
Unit cell dimensions (Å)					
a	5.2307	5.2335	5.1083	5.211	5.1490
b	5.2903	5.3020	5.1695	5.286	5.2075
c	5.3943	5.3785	5.2717	5.388	5.3158
β	99.451	99.508	99.21	99.59	99.228
Atom Coordinates					
Zr					
x	0.2752	0.2757	0.2769	0.277	0.2753
y	0.0414	0.0420	0.0422	0.043	0.0390
z	0.2098	0.2092	0.2097	0.210	0.2093
O_1					
x	0.0697	0.0719	0.0689	0.070	0.0670
y	0.3336	0.3385	0.3333	0.336	0.3286
z	0.3461	0.3418	0.3445	0.343	0.3455
O_2					
x	0.4524	0.4522	0.4495	0.450	0.4558
y	0.7580	0.7586	0.7573	0.758	0.7586
z	0.4794	0.4809	0.4798	0.478	0.4768

With the aid of Moldraw, the bond lengths and angles were calculated and in comparison with the values (Table 3) from the calculations by Zhao and Vanderbilt and measurements by McCullough and Trueblood's. The calculated numbers in this work are all within the range of the experimental standard deviations.

Table 3: Bond lengths and angles

Distance (Å)	B.S. B	LDA[13]	Expt[3] (σ ≈ .05Å)	Angle (°)	B.S. B	LDA[13]	Expt[3] (σ ≈ 2°)
Zr – O_1							
D1	2.09	2.04	2.04	θ_{12}	145	139	145
D2	2.09	2.05	2.10	θ_{13}	110	106	109
D3	2.18	2.14	2.15	θ_{23}	105	105	106
Zr – O_2							
D1	2.19	2.14	2.16	θ_{12}	108	109	109
D2	2.28	2.23	2.26	θ_{13}	107	106	107
D3	2.21	2.15	2.18	θ_{14}	132	133	132
D4	2.30	2.23	2.26	θ_{23}	102	102	102
				θ_{24}	100	101	100
				θ_{34}	104	104	104

Based on these preliminary calculations, the B.S. B and the B3LYP functional used are able to properly predict the geometric structure of the monoclinic phase of ZrO_2 at room temperature and will be used in the vibrational analysis.

Frequency Calculations

As a means of characterization, Raman spectroscopy has the advantage over other types of spectroscopy because it is well defined and is also sensitive to local symmetry and the changes in the oxygen sub-lattice[6,33,34]. For this reason, the focus of the comparison and calculations is on the Raman active modes of monoclinic ZrO_2. Based on the space group of ZrO_2, there are 18 expected Raman peaks for this monoclinic phase represented in the irreducible form as $9A_g + 9B_g$. There have been numerous experimentally determined Raman spectroscopy and these were summarized in Table 1 of Kim and Hamaguchi's paper[8]. Table 4 shows some of the values presented in that paper along with Feinberg and Perry's earlier work. The mean Raman peaks are calculated for use in comparing the differences between

calculated and measured frequencies, while the symmetry from these modes were assigned based on Ishigame and Sakurai's[5] as well as Feinberg and Perry's[6] assignments.

Table 4 Experimentally determined Raman modes

Phillipi[35]	Feinberg[6]		Ishigame[5]		Carlone[16]	Anastassaki[4]	Kim[8]		Overall		
ω (cm^{-1})	ω (cm^{-1})	Symm	ω (cm^{-1})	Symm	ω (cm^{-1})	ω (cm^{-1})	ω (cm^{-1})	Assignment	ω (cm^{-1})	St. Dev	Symm
	92	B_g				92					
104	102	A_g	102	A_g	99	101	105	O-O	102	2	A_g
	148	B_g									
180	179	A_g	179	$A_g + B_g$	177	177	180	Zr-Zr	179	1	A_g
192	190	A_g	190	A_g	189	189	192	Zr-Zr	190	1	A_g
223	222	B_g	222	B_g	222	222	224	Zr-Zr	223	1	B_g
					270						
307	305	A_g	305	A_g	305	306	308	Zr-O	306	1	A_g
						315					
337	334	B_g	334	B_g	331	335	334	Zr-Zr	334	2	B_g
348	348	A_g	348	A_g	343	347	349	Zr-O	347	2	A_g
						355					
					376		380	Zr-O			
382	381	B_g	381	B_g	376	382	385	O-O	381	3	B_g
476	476	A_g	476	A_g	473	476	476	O-O	476	1	A_g
502	500	B_g	500	B_g	498	502	503	O-O	501	2	B_g
538	534	B_g	534	B_g	534	537	539	O-O	536	2	B_g
559	556	A_g	556	A_g	557	559	558	O-O	558	1	A_g
617	615	$2B_g$	615	B_g	613	616	616	O-O	615	1	B_g
638	637	$2A_g$	637	A_g	633	637	638	O-O	637	2	A_g
					705						
					780	764	757	O-O			

Previously calculated vibrational frequencies using LDA and GGA functional are shown in Table 5 with the mean difference being used as an evaluation of accuracy. The frequency difference is calculated by equation 1 and the average differences are -4, -20 and 15cm^{-1} for LDA, GGA and B3LYP using the mean frequencies from Table 4 as the reference frequencies

$$\Delta = \omega_{\text{calculated}} - \omega_{\text{reference}} \quad [1]$$

In general, the LDA calculations overestimated at lower frequencies (< 330 cm^{-1}) and underestimated at higher frequencies while the GGA calculations underestimated the Raman peaks. On the other hand, the B3LYP calculation generally overestimated the Raman peaks. This agrees with previous experiments which found that as temperature increases, there was a red shift with respect to frequency hence lower temperatures would produce a blue shift with respect to the experimental Raman peaks. In addition, Ishigame & Sakurai found that the peaks also broadened as temperature was increased between 300K and 1250K and the reverse occurred upon decreasing temperature. This also appears to explain the reason why some of the peaks are not observable at room temperature in most experiments i.e. peaks at 182cm^{-1}, 328cm^{-1}, 394cm^{-1} and 775cm^{-1} (B3LYP).

Table 5 Comparison between accepted experimental and calculated Raman modes

Average		B3LYP			LDA			GGA		
ω (cm^{-1})	Sym	ω (cm^{-1})	Sym	Δ	ω (cm^{-1})	Sym	Δ	ω (cm^{-1})	Sym	Δ
102	A_g	74	A_g	-28	103	A_g	1	108	A_g	6
		182	B_g		175	B_g		162	B_g	
179	A_g	182	A_g	3	180	A_g	1	169	A_g	-10
190	A_g	199	A_g	8	190	A_g	0	179	A_g	-11
223	B_g	226	B_g	4	224	B_g	2	216	B_g	-7
		328	B_g		313	B_g		293	A_g	
305	A_g	340	A_g	35	317	A_g	12	303	B_g	-2
334	BG	351	B_g	17	330	B_g	-4	316	B_g	-18
347	A_g	364	A_g	16	345	A_g	-2	324	A_g	-23
381	BG	387	B_g	6	382	B_g	1	371	B_g	-10
		394	A_g		381	A_g		371	A_g	
476	A_g	487	A_g	12	466	A_g	-10	453	A_g	-23
501	BG	509	B_g	8	489	B_g	-12	473	B_g	-28
536	BG	570	BG	34	533	BG	-3	512	BG	-24
558	AG	574	AG	17	548	AG	-10	524	AG	-34
615	BG	638	BG	22	601	BG	-14	580	BG	-35
637	AG	651	AG	14	631	AG	-6	605	AG	-32
		775	BG		748	BG		719	BG	
Average Difference		12			-3			-20		

The temperature effect on Raman spectra is reinforced by Carlone's paper where the peak observed at 780 cm^{-1} was stronger at 15K (more intense) yet almost unobservable at 300K[16].

A visual comparison between Carlone's Raman spectrum at 300K (Figure 1) and the B3LYP calculated spectrum is shown in Figure 2. Carlone's spectrum was obtained by digitizing the aforementioned figure using GetData Graph Digitizer[36], while the B3LYP spectrum was obtained by digitizing the Lorentzian convolution obtained from Moldraw. This again shows how well the hybrid functional predicts the Raman spectrum for the monoclinic phase even at low temperatures. It should be noted that CRYSTAL has not been fully developed to handle the prediction of Raman intensities. Notwithstanding, it is still evident that the peaks experience a red shift for reasons previously mentioned.

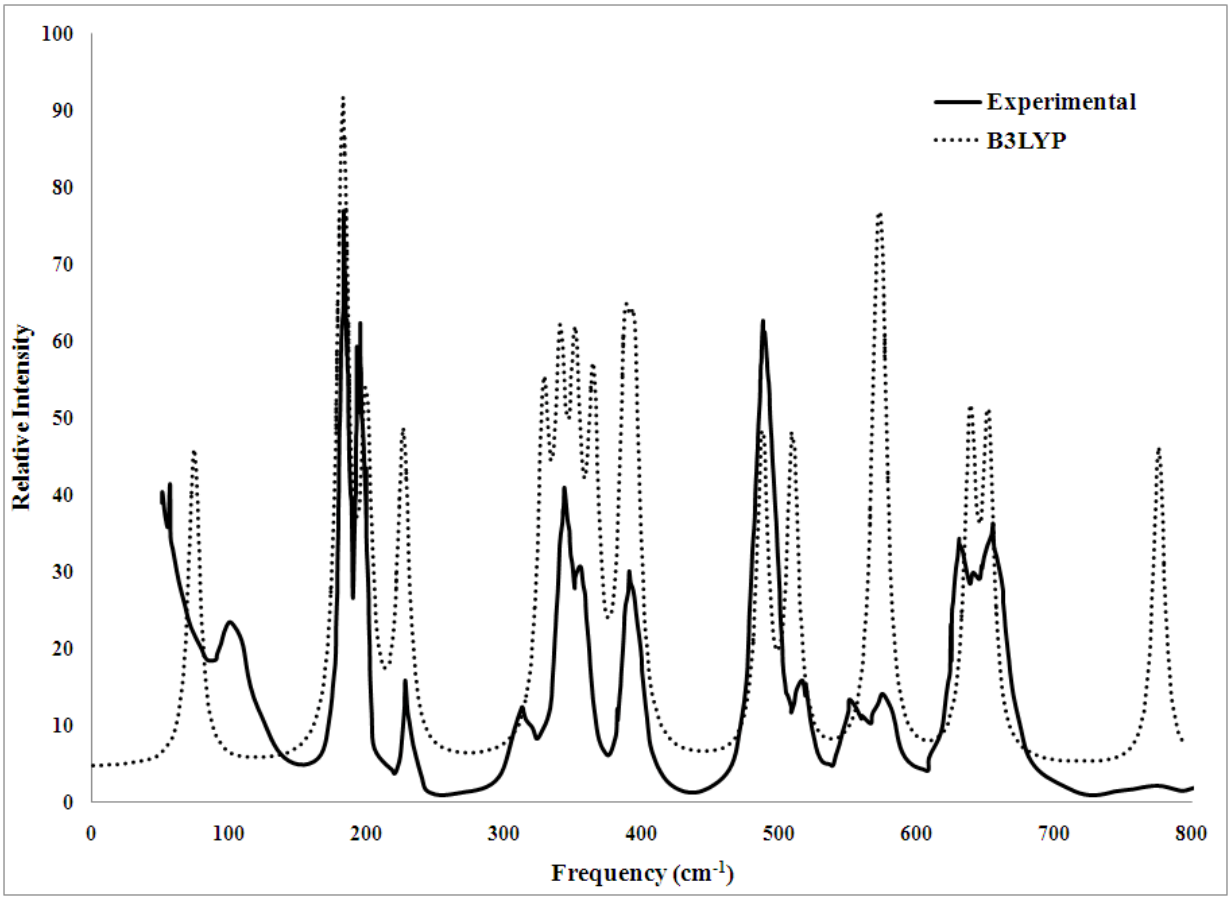

Figure 2 Comparison between experimental and B3LYP calculated Raman spectrum of monoclinic ZrO_2.

An attempt was also made to investigate the effect of unit cell size on Raman calculations and this was done using Gaussian 03. Although Gaussian is unable to perform frequency analysis under periodic boundary conditions, an initial starting structure using the experimental geometry was created and then frequency calculations were performed on a geometrically optimized structure. This was also repeated using 2 and 3 unit cells resulting in 8 and 12 formula units of ZrO_2. This investigation found the results improved as the size of the unit cell was increased. As can be seen in Figure 3, higher frequencies peaks were observed to match up with experimental peaks for example at 561 cm^{-1}, 591 cm^{-1}, 627 cm^{-1} and 658 cm^{-1}. This suggests that even when these periodic conditions are not maintained, the frequency modes can be better estimated by increasing the amount of molecules chosen to represent the system. Obviously there is a tradeoff with regards to accuracy and system size.

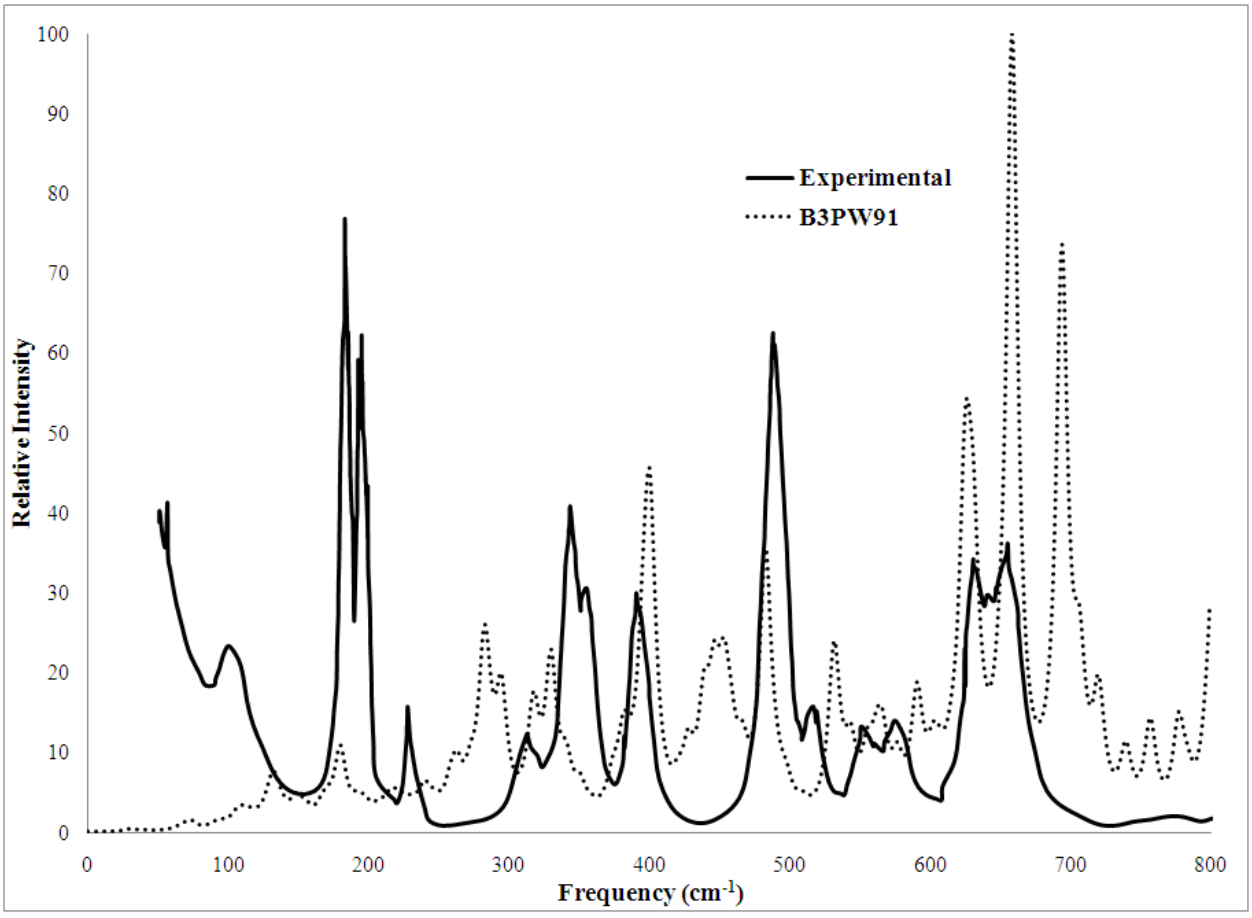

Figure 3 Comparison between experimental and 3-unit cell generated Raman spectrum

Conclusions

The initial analysis in comparing the theoretical and experimental geometry of a unit cell of zirconia showed that the pseudopotential and basis set used for Zr and O as well as the hybrid functional used were able to predict the structure of the monoclinic phase and therefore were expected to perform well for the frequency calculations. Based on the Raman spectra obtained from a series of experiment at room temperature, the 0K calculations were a good representation of the system. A blue shift and narrowing of peaks is expected for the calculations since high temperatures were found to decrease frequency values and broaden peaks. In addition, an increase in the size of the system studied generated more accurate spectra when periodic conditions were not enforced as was shown in the case of Gaussian 03

Based on the performance of the basis set and functional used, a foundation has been set up for using quantum chemistry as a method to investigate the performance of typical solid oxide fuel cell components using frequency analysis that can be further validated experimentally. In other words, the agreement with experimental frequency values is evidence of the ability of the calculations to further highlight the characteristics of zirconium oxide in the monoclinic phase and this can be extended to the stabilized cubic phase as well.

Acknowledgements

This work was supported by the Department of Energy (award number DE-FG26-05NT42527). This work was also supported in part by an allocation of computing time from the Ohio Supercomputer Center.

References

1. Ryshkewitz, E. Oxide ceramics : physical chemistry and technology; Academic Press: New York :, 1960.

2. Orlando, R.; Pisani, C.; Ruiz, E.; Sautet, P. Surf Sci 1992, 275(3), 482-492.

3. McCullough, J. D.; Trueblood, K. N. Acta Crystallographica 1959, 12(7), 507-511.

4. Anastassakis, E.; Papanicolaou, B.; Asher, I. M. J Phys Chem Solids 1975, 36, 667-676.

5. Ishigame, M.; Sakurai, T. J Am Ceram Soc 1977, 60(7 - 8), 367 - 369.

6. Feinberg, A.; Perry, C. H. J Phys Chem Solids 1981, 42(6), 513-518.

7. Bondars, B.; Heidemane, G.; Grabis, J.; Laschke, K.; Boysen, H.; Schneider, J.; Frey, F. J Mater Sci 1995, 30(6), 1621-1625.

8. Kim, B. K.; Hamaguchi, H. O. Phys Status Solidi B-Basic Res 1997, 203(2), 557-563.

9. Dewhurst, J. K.; Lowther, J. E. Phys Rev B 1998, 57(2), 741-747.

10. Gennard, S.; Cora, F.; Catlow, C. R. A. J Phys Chem B 1999, 103(46), 10158-10170.

11. Jomard, G.; Petit, T.; Pasturel, A.; Magaud, L.; Kresse, G.; Hafner, J. Phys Rev B 1999, 59(6), 4044-4052.

12. Kuwabara, A.; Tohei, T.; Yamamoto, T.; Tanaka, I. Phys Rev B 2005, 71(6).

13. Zhao, X. Y.; Vanderbilt, D. Phys Rev B 2002, 65(7).

14. Christensen, A.; Carter, E. A. Phys Rev B 1998, 58(12), 8050-8064.

15. Kohanoff, J. Electronic structure calculations for solids and molecules : theory and computational methods; Cambridge University Press: Cambridge, UK ; New York :, 2006.

16. Carlone, C. Phys Rev B 1992, 45(5), 2079-2084.

17. Ralph, J. M.; Schoeler, A. C.; Krumpelt, M. J Mater Sci 2001, 36(5), 1161-1172.

18. Marquez, A. I.; De Abreu, Y.; Botte, G. G. Electrochem Solid State Lett 2006, 9(3), A163-A166.

19. Dovesi, R.; Saunders, V. R.; Roetti, C.; Orlando, R.; Zicovich-Wilson, C. M.; Pascale, F.; Civalleri, B.; Doll, K.; Harrison, N. M.; Bush, I. J.; D'Arco, P.; Llunell, M. CRYSTAL06 User's Manual: University of Torino, Torino, 2006.

20. Frisch, M. J.; Trucks, G. W.; Schlegel, H. B.; Scuseria, G. E.; Robb, M. A.; Cheeseman, J. R.; Montgomery, J., J. A.; Vreven, T.; Kudin, K. N.; Burant, J. C.; Millam, J. M.; Iyengar, S. S.; Tomasi, J.; Barone, V.; Mennucci, B.; Cossi, M.; Scalmani, G.; Rega, N.; Petersson, G. A.; Nakatsuji, H.; Hada, M.; Ehara, M.; Toyota, K.; Fukuda, R.; Hasegawa, J.; Ishida, M.; Nakajima, T.; Honda, Y.; Kitao, O.; Nakai, H.; Klene, M.; Li, X.; Knox, J. E.; Hratchian, H. P.; Cross, J. B.; Bakken, V.; Adamo, C.; Jaramillo, J.; Gomperts, R.; Stratmann, R. E.; Yazyev, O.; Austin, A. J.; Cammi, R.; Pomelli, C.; Ochterski, J. W.; Ayala, P. Y.; Morokuma, K.; Voth, G. A.; Salvador, P.; Dannenberg, J. J.; Zakrzewski, V. G.; Dapprich, S.; Daniels, A. D.; Strain, M. C.; Farkas, O.; Malick, D. K.; Rabuck, A. D.; Raghavachari, K.; Foresman, J. B.; Ortiz, J. V.; Cui, Q.; Baboul, A. G.; Clifford, S.; Cioslowski, J.; Stefanov, B. B.; Liu, G.; Liashenko, A.; Piskorz, P.; Komaromi, I.; Martin, R. L.; Fox, D. J.; Keith, T.; Al-Laham, M. A.; Peng, C. Y.; Nanayakkara, A.; Challacombe, M.; Gill, P. M. W.; Johnson, B.; Chen, W.; Wong, M. W.; Gonzalez, C.; Pople, J. A.; Gaussian, Inc.: Wallingford CT, 2004.

21. Becke, A. D. Journal of Chemical Physics 1993, 98(7), 5648-5652.

22. Lee, C. T.; Yang, W. T.; Parr, R. G. Phys Rev B 1988, 37(2), 785-789.

23. Montanari, B.; Civalleri, B.; Zicovich-Wilson, C. M.; Dovesi, R. Int J Quantum Chem 2006, 106(7), 1703-1714.

24. Pascale, F.; Zicovich-Wilson, C. M.; Orlando, R.; Roetti, C.; Ugliengo, P.; Dovesi, R. J Phys Chem B 2005, 109(13), 6146-6152.

25. Prencipe, M.; Noel, Y.; Civalleri, B.; Roetti, C.; Dovesi, R. Phys Chem Miner 2006, 33(8-9), 519-532.

26. CRYSTAL. http://www.crystal.unito.it/Basis_Sets/zirconium.html, Ed., 2008.

27. Bredow, T. Phys Rev B 2007, 75(14).

28. Ugliengo, P.; Viterbo, D.; Chiari, G. Zeitschrift Fur Kristallographie 1993, 207, 9-23.

29. Ugliengo, P.; Torino, 2006.

30. Frisch, A.; Frisch, M. J.; Trucks, G. W. Gaussian 03 User's Reference Gaussian, Inc.: Carnegie, PA :, 2003.

31. Dennington II, R.; Keith, T.; Millam, J.; Eppinnett, K.; Hovell, W. L.; Gilliland, R.; Semichem, Inc.: Shawnee Mission, KS, 2003.

32. McCarthy, M. I.; Harrison, N. M. Phys Rev B 1994, 49(13), 8574-8582.

33. Calderon-Moreno, J. M.; Yoshimura, M. Solid State Ionics 2002, 154, 125-133.

34. Lopez, E. F.; Escribano, V. S.; Panizza, M.; Carnasciali, M. M.; Busca, G. J Mater Chem 2001, 11(7), 1891-1897.

35. Phillippi, C. M.; Mazdiyasni, K. S. J Amer Ceram Soc 1971, 54(5), 254-258.

36. Fedorov, S.; http://getdata-graph-digitizer.com/: Moscow, Russia, 2008.